

Microbubble Generation from Condensation and Turbulent Breakup of Sheet Cavitation

P. S. Russell, D. R. Giosio, J. A. Venning, B. W. Pearce, P. A. Brandner
(Australian Maritime College, University of Tasmania, Australia),
S. L. Ceccio (Department of Naval Architecture and Marine Engineering,
University of Michigan, USA)

ABSTRACT

The formation, size and concentration of microbubbles generated in the wake of a cavitating hydrofoil are investigated experimentally for several Reynolds and cavitation numbers. The present work is restricted to bubble generation from stable sheet cavitation. Interactions between the cavity, the overlying boundary layer and associated interfacial effects are investigated qualitatively and quantitatively using high-resolution and high-speed photography. The physics of cavity breakup and condensation and microbubble formation are also investigated using high-speed photography. Size and concentration of microbubble populations are measured in the far wake using diffused laser shadowgraphy. The optical setup of the shadowgraphy permitted microbubbles in the size range of 5 to 300 μm to be resolved. Coherent spatial and temporal features of the sheet cavitation are shown to be functions of both Reynolds and cavitation numbers. For the range of microbubble sizes measured, concentrations are shown to increase with Reynolds number and reduce with decreasing cavitation number. In contrast, void fraction increases with decreasing cavitation number indicating a greater production of larger diameter bubbles.

INTRODUCTION

Dispersed bubbly flows generated or modulated by ships and submarines may persist for a long period of time following the passing of a vessel. In addition to background populations, ships are prolific sources of polydisperse bubble populations due to the significant surface disturbances and turbulence they generate. Considerable volumes of air

are ingested and dispersed about the hull and by the propulsion and control equipment. Various mechanisms are involved including plunging jets and captured air volumes generated by breaking waves as described by Castro, et al. (2014), while surface turbulence may also be sufficient for the hull boundary layer to entrain air (Washuta, et al., 2014; Kim, et al., 2014). Lifting surfaces are also of interest here in regards to cavitation occurrence and the consequent contribution to microbubble generation (Yu and Ceccio, 1997). New insights into the dynamics of developed cavitation are being gained both experimentally (Brandner, et al., 2010a; Ganesh, et al., 2014), and numerically (Gnanaskandan and Mahesh, 2014), however, the mechanisms by which cavitating flows generate microbubbles remain largely to be investigated.

As the techniques advance, Computational Fluid Dynamics (CFD) is being used to model fluid flows of increasing complexity, including in the area of turbulent multiphase flow prediction (Balachandar and Eaton, 2010; Fox, 2012). Recent numerical work specifically on turbulent cavitating flows has been reported by Gnanaskandan and Mahesh (2015). These numerical techniques all involve some use of modelling, particularly at small scales, so the flow physics is only captured accurately to varying degrees. While CFD provides valuable detailed full field information, careful comparison with experimental data is required to ensure fidelity. In many aspects numerical techniques have currently progressed ahead of available experimental data.

The numerical calculation of the full flow field about cavitating hydrofoils and propellers has been developing, in particular since the early

1990's, with ongoing interest in the topic (e.g. Huang, et al., 2013; Ji, et al., 2013, 2015). Qin, et al. (2003a,b) reported on the unsteady turbulent far wake behind a cavitating hydrofoil. While gross flow effects were adequately simulated, it was found that only when the effect of dissolved gas content was included in the numerical model, local quantities such as the wake velocity distributions were captured accurately. This was also the case in an earlier study by Kjeldsen, et al. (2000), where deviations in the numerical flow prediction downstream of a foil were linked to dissolved gas content in the wake.

There are limited reported experimental surveys of the bubble distribution within the wake of a cavitating hydrofoil. Maeda, et al. (1991) investigated the microbubble population within cloud cavitation occurring about a NACA 0015 hydrofoil (Reynolds number (Re) – 6.2×10^5 , cavitation number (σ) – 1.96, incidence (α) – 8.36° and a dissolved oxygen content of 10 to 15%). The dominant bubble size was found to be of the order of 10 to 20 μm . Yu and Ceccio (1997) reported similar size distributions at a single measurement point within the turbulent wake of two cavitating wedges at $Re = 1.1 \times 10^5$ and σ between 1.5 and 1.6, for an oxygen content of 27%. More recently, de Graaf, et al. (2014) performed a spatial survey in the wake of a modified NACA 63A015 hydrofoil at a single operating condition of $Re = 0.5 \times 10^6$, $\sigma = 0.37$, and $\alpha = 3.5^\circ$, and found the dominant bubble size to vary in the spanwise and streamwise (at mid-span) directions between 25 and 40 μm .

A related study on the effect of freestream velocity on the bubble size distribution within the wake of a non-cavitating, ventilated NACA 0015 hydrofoil was reported by Karn, et al. (2015). Two bubble size 'modes' were observed, the more dominant being of the order of 300 μm , while the second mode was around 620 μm . As the Re was varied from 2.4×10^5 to 8.1×10^5 the probability density function of the first mode was found to increase while the second decreased. The Sauter mean diameter was also shown to decrease with increasing Re . The local physics of bubble breakup and coalescence is complex (Liao and Lucas, 2009, 2010) and the relative contributions of these processes to

resultant bubble distributions in the wake of cavitating or ventilated bodies is a focus of current research.

Microbubbles respond dynamically to the changing pressure field about a hydrofoil resulting in an uneven diffusion during advection which remains to be fully understood. Not only is the size of the bubble important but the velocity of the bubble relative to that of the surrounding fluid. Given a sufficient velocity difference smaller bubbles can grow from their initial radius by an order of magnitude (Smith and Peterson, 1984). This emphasises the importance of eliminating free stream microbubble content when investigating wake bubble size distributions produced from cavitation. As discussed in the following section the facility used in the present study has the capability for control of the dissolved gas content and removal of all free bubbles from the incoming freestream.

The aim of the present study is to gain a more detailed understanding of sheet cavity formation and breakup physics, including the resultant microbubble population in the downstream wake, for a range of flow conditions. The findings, as part of an ongoing study, are expected to serve as data for comparison and validation of numerical models for the prediction of these types of flows.

EXPERIMENTAL APPROACH

Experiments were carried out in the Cavitation Research Laboratory (CRL) variable pressure water tunnel at the University of Tasmania. A schematic of the facility architecture with a description of the main features is shown in Figure 1. The tunnel test section is 0.6 m square by 2.6 m long in which the operating velocity and pressure ranges are 2 to 12 m/s and 4 to 400 kPa absolute, respectively. The tunnel volume is 365 m^3 , which is filled with demineralised water (conductivity of order 1 $\mu\text{S}/\text{cm}$).

The tunnel has ancillary systems for rapid degassing and for continuous injection and removal of nuclei and large volumes of incondensable gas. The test section velocity is measured from one of two (low and high range) Siemens Sitrans P differential pressure transducers models

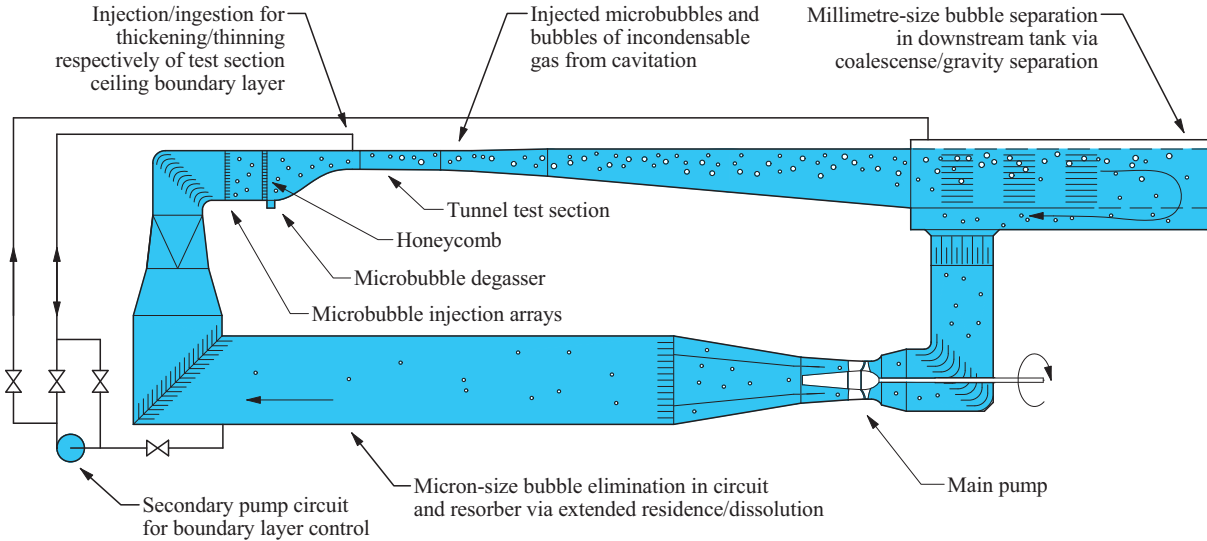


Figure 1. Schematic of the CRL water tunnel circuit. The facility is designed for continuous injection and separation of in-condensable gas and cavitation nuclei via processes of coalescence/gravity separation of bubbles greater than about 100 μm in a downstream tank and dissolution with extended residence in the lower limb or resorber.

7MF4433-1DA02-2AB1-Z and 7MF4433-1FA02-2AB1-Z (measuring the calibrated contraction differential pressure) with estimated precision of 0.007 m/s and 0.018 m/s, respectively. The velocity and pressure in the test section are controlled to maintain a constant Re and σ . The test section velocity is spatially uniform to within $\pm 0.5\%$, has temporal variations of less than 0.2%, and the free stream turbulent intensity is about 0.5%. Detailed descriptions of the facility are given in Brandner, et al. (2006, 2007) and Doolan, et al. (2013).

An anodized aluminium hydrofoil was mounted on the test section ceiling centreline, as shown in Figure 2, 1.15 m downstream from the entrance. The hydrofoil geometry consisted of an elliptical planform, with a span of 200 mm, a base-chord length (i.e. the chord length at the hydrofoil/window junction) of 120 mm, and a modified NACA 63A015 profile. The profile modification involved an increase of the trailing edge thickness (see Figure 3) to enable practical manufacture of the scaled model and to reduce susceptibility to in-service trailing edge damage. The modified profile was achieved by the addition of $0.00385x$ to the standard profile, where x is the chord-wise distance from the leading edge .

High-resolution (36.3 megapixel) still photographs were captured using a Nikon D800E DSLR with a Nikon AF-S Micro Nikkor 105 mm 1:2.8G ED lens. Illumination was provided by two simultaneously triggered stroboscopes, a Drello 3018 scope with 4037 flashlamp and a Drello 1018 scope with 4040 flashlamp. High-speed photographic images were acquired at 14,000 Hz using a LaVision HighSpeedStar8 CMOS 12-bit 1 megapixel camera with a Nikon AF Nikkor 50 mm 1:1.4D lens. A combination of high powered LED light units including 2 custom-made lamps (based on the Cree XLamp CXA3050 LED) and a Veritas Constellation 120 W light source were used to obtain sufficient illumination.

Shadowgraph images were acquired using a LaVision Imager LX 12-bit 29M camera in combination with a Questar QM100 long-range microscope. The camera CCD sensor size is 6600×4400 pixels. The long-range microscope was coupled to the camera using a $3\times$ Barlow lens giving a field of view of $1917 \mu\text{m} \times 1279 \mu\text{m}$ with a spatial resolution of $0.29 \mu\text{m}/\text{px}$. This optical set-up allows a range of bubble sizes from 5 to 300 μm to be measured with a 5 μm bubble being imaged with 17 pixels across the diameter. The lower size

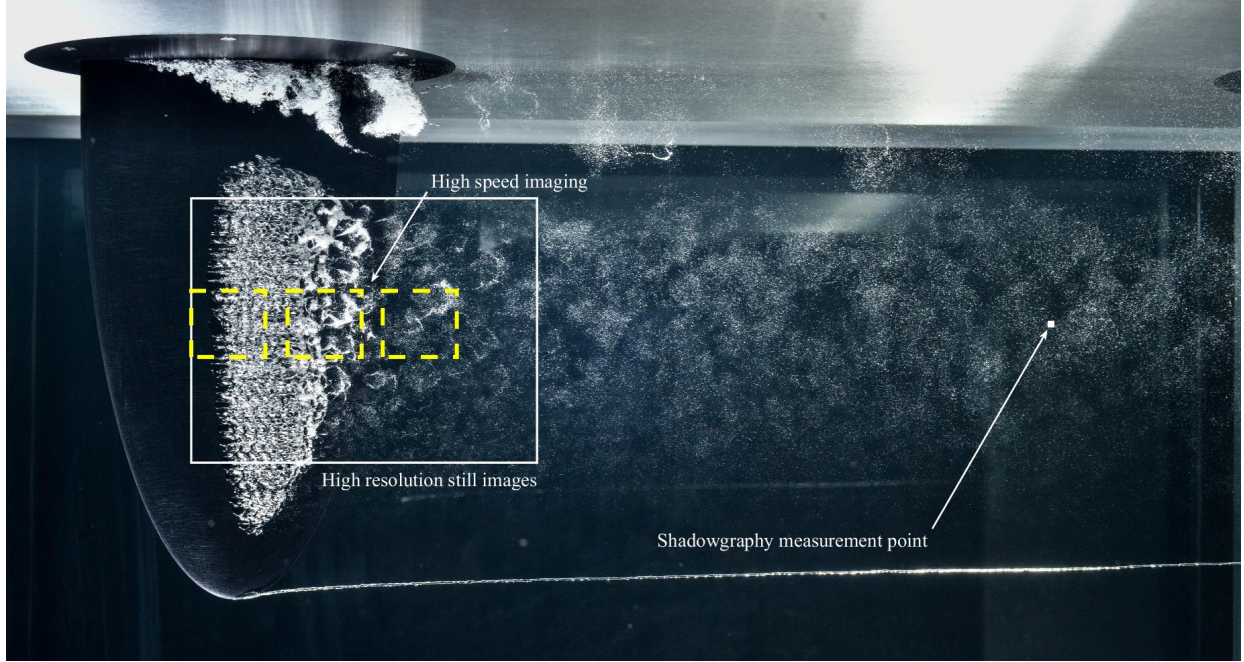


Figure 2. Elliptical planform modified NACA 63A015 section hydrofoil mounted in the CRL water tunnel. The location of the shadowgraphy measurement point is at mid-span, $2.5 \times$ the root chord length downstream from mid-chord. The field of view for the high-resolution stills is indicated by the solid white boundary, while high-speed imaging field of views are given by the dashed yellow boundaries.

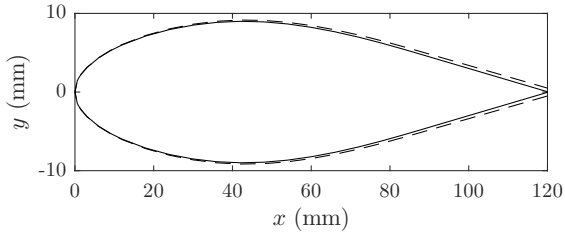


Figure 3. Comparison of a standard (solid) and modified (dashed) NACA 63A015 section. The modification thickens the profile gradually from the leading edge through to a maximum at the trailing edge.

is limited by the spatial resolution and the diffraction limit while the upper size is limited by the field of view and depth of field. One thousand images per data point were acquired based on the number required for converged statistics found from an earlier study (Brandner, et al., 2010b).

To improve the optical access the 110 mm acrylic test section side window was replaced by a stainless steel window fitted with a 160 mm diameter, 79.5 mm thick, glass port. Backlit illumina-

tion was provided by a Litron Nano L PIV Nd:YAG laser (532 nm, 120 mJ, 20 Hz) guided through a LaVision high efficiency diffuser using a fluorescent dye plate. A cone of diffused light was produced which emitted pulses in the wavelength range 574 to 580 nm and of 20 ns duration when excited by 5 ns, 532 nm laser pulses. Both the camera and diffuser were affixed to Linos optical rails and mounted on Isel 3-axis (790 mm) linear traverses to allow accurate alignment and positioning. The laser and camera were triggered from a programmable timing unit and the acquisition and bubble sizing analysis was carried out using LaVision DaVis Version 8.3.0.

All data were obtained at a fixed incidence of 3.5° and at several chord-based Reynolds numbers, $Re = Uc/\nu$ (where U is the free stream velocity, c the root-chord length and ν the kinematic viscosity), and cavitation numbers, $\sigma = (p - p_v)/(1/2\rho U^2)$ (where p is the freestream static pressure at the mid-span of the hydrofoil, p_v the vapour pressure, and ρ the density of the fluid). The dissolved oxygen content was maintained be-

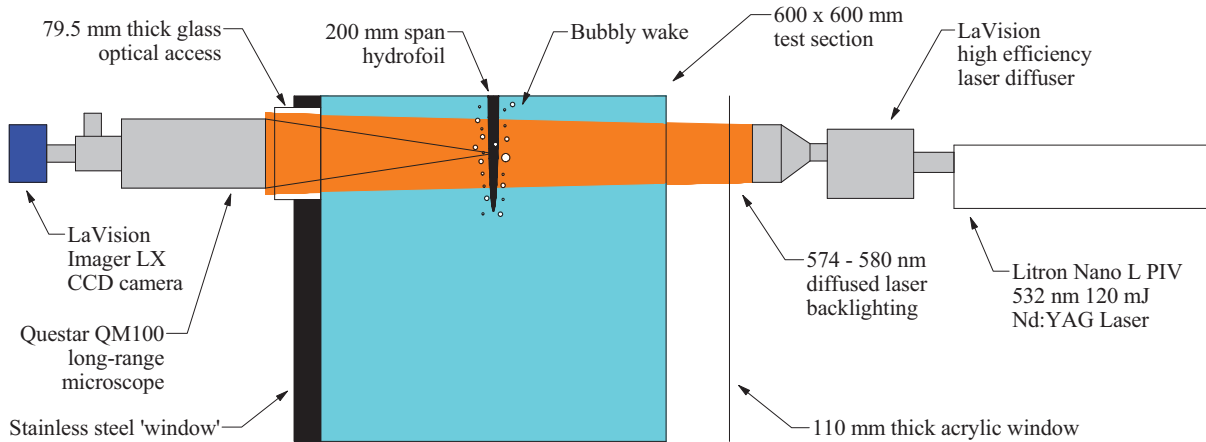


Figure 4. Schematic of experimental set-up for diffused laser shadowgraphy measurement in the wake of a hydrofoil in the CRL water tunnel test section (transverse view looking upstream).

tween 2.5 and 3 ppm for all test conditions.

RESULTS

Cavity geometry and topography

A set of high-resolution photographs of cavitation development about the hydrofoil at $\alpha = 3.5^\circ$ for a range of Re and σ values are presented in Figure 5. For $Re = 1.05 \times 10^6$, inception occurs just above $\sigma = 0.35$ and this value was observed to increase slightly with increasing Re . It was found that a cavity could not be sustained at $\sigma = 0.35$ for $Re < 1.05 \times 10^6$.

The cavity length (streamwise extent) and width (spanwise extent) increase with decreasing σ and also with increasing Re . Although not systematically investigated, the cavity width extends to the hydrofoil tip for sufficiently low σ and/or high Re . The effect of Re on cavity length is greatest for the higher σ values, as shown in Figure 5. Photographs acquired for a large range of Re values (not presented) suggest that the cavity length tends to converge with an increasing Re and/or a decreasing σ . A similar trend is also observed for the cavity leading edge that moves upstream with decreasing σ and increasing Re . The effect of Re increase from 0.6×10^6 to 1.5×10^6 for $\alpha = 3.5^\circ$ and $\sigma = 0.25$ on the cavity geometry and topography may be seen from the cropped photographs, with a constant field of view, shown in Figure 6. A direct comparison of

photographs for the largest and smallest Re values is also shown in Figure 7, with the same magnification. The leading-edge movement between these Re values is about 10 mm, or 10% of the local chord.

Length scales of cavity topographical features generally change significantly with Re as is evident from the photographs shown in Figures 5 to 7. Despite these changes, the overall cavity physics are similar. The cavity leading edge is composed of laminar cells resulting from a complex interaction between the separating unstable laminar boundary layer and interfacial effects at the liquid-gas-solid juncture at cavity detachment. The occurrence of these leading edge cells on sheet and cloud cavitation have been reported on by e.g. Tassin Leger, et al. (1998) and Brandner, et al. (2010a).

Spanwise waves on the cavity surface in the wake of each cell are evident in the photographs. These are due to the Kelvin-Helmholtz (KH) instability in the overlying boundary layer. Spanwise discontinuities or edge effects in the surface waves corresponding with the divots separating the cells show these to induce three dimensional effects on the KH waves. The waves persist to the cavity trailing edge and drive coherent breakup and vortical cavity formation of the same length scale as the leading-edge cells. With downstream advection and condensation, these cavitating hairpin shaped vortices reduce in volume and ultimately break up into microbubbles of incondensable gas in the far wake.

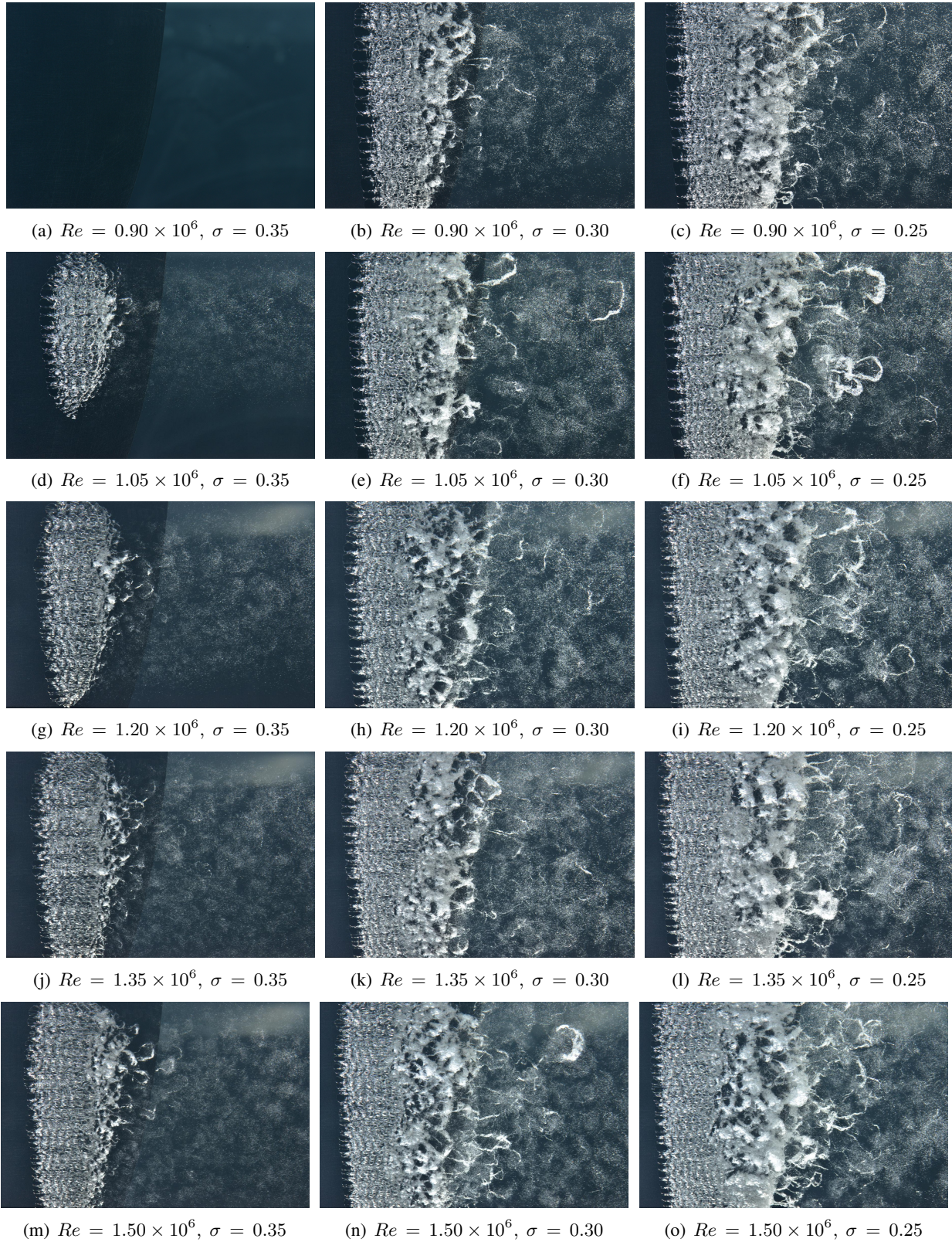


Figure 5. High-resolution photography of attached sheet cavitation on a modified NACA 63A015 section elliptical platform hydrofoil for various operating conditions. Flow is from left to right.

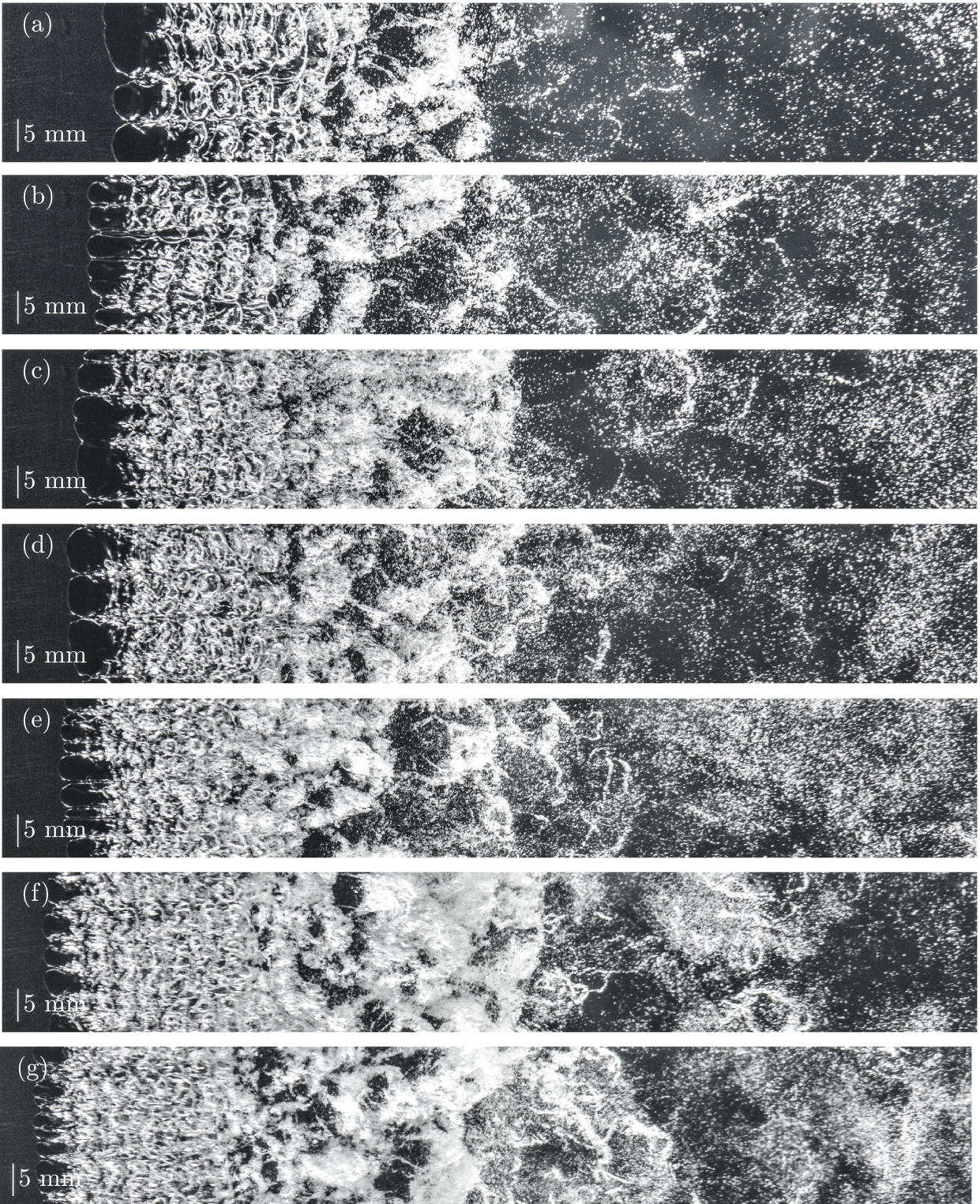
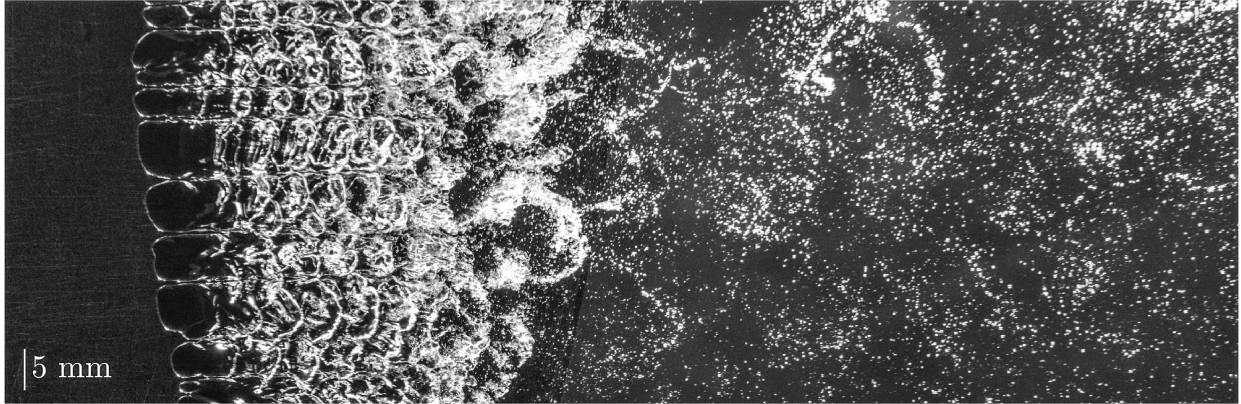
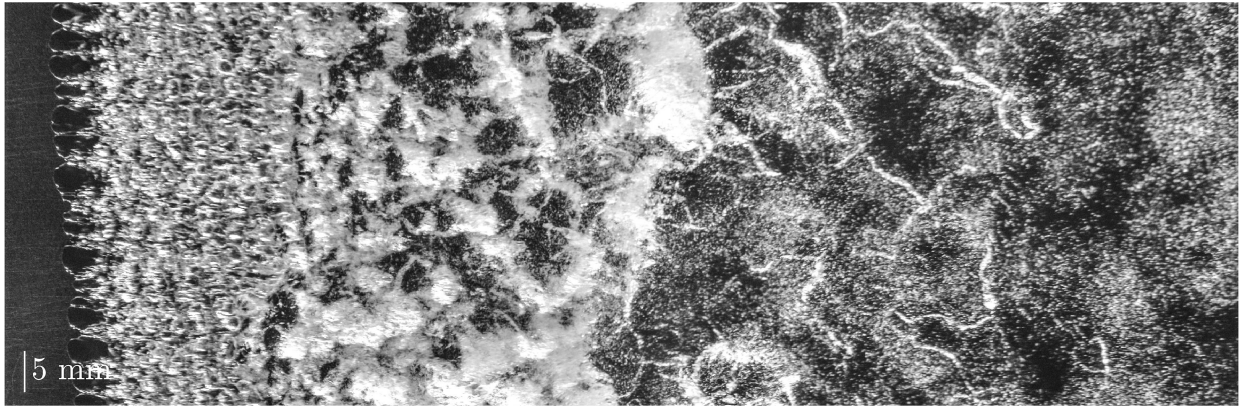


Figure 6. High-resolution photography of the variation of cavity leading-edge geometry as a function of Re . All photographs are at $\sigma = 0.25$. (a) $Re = 0.6 \times 10^6$, (b) $Re = 0.7 \times 10^6$, (c) $Re = 0.8 \times 10^6$, (d) $Re = 0.9 \times 10^6$, (e) $Re = 1.05 \times 10^6$, (f) $Re = 1.3 \times 10^6$, and (g) $Re = 1.5 \times 10^6$.



(a) $Re = 0.6 \times 10^6$, $\sigma = 0.25$



(b) $Re = 1.5 \times 10^6$, $\sigma = 0.25$

Figure 7. Comparison of two photographs showing the effect of Re on cell size and wavelength. The σ is constant between the two cases. In the top image, the average cell span is 5.1 mm, the average cell length is 5.1 mm, and the average wavelength is 4.7 mm. In the bottom image at higher Re , the average cell span is 3.4 mm, the cell length is 5.1 mm, and the wavelength is 3.4 mm.

From the high resolution photographs, it can be seen qualitatively that the length and width of the leading edge cells decrease with increasing Re . The wavelength of the KH waves also decreases with increasing Re (Figure 7). From Figure 7, it can be seen that the continuous cavity length is similar for each Re but the breakup region is much longer and the number and volume of shed cavitating vortices is much greater for the higher Re case. The vortices also persist much further downstream for the higher Re case before eventual condensation and breakup into microbubbles. Perhaps most significant is the difference in size and concentration of the generated microbubbles with the change in Re . At the low Re , low concentrations of apparently large bubbles are generated in comparison with the high Re case where much higher concen-

trations of bubbles are generated with a greater size distribution. The geometric and topographical features discussed here qualitatively are further analyzed quantitatively below using data derived from the high-resolution photography, high-speed photography and the wake shadowgraphy.

Scaling and dynamic behaviour of cavity topographical features

The variation of the leading-edge cell mean width, s , with Re and σ has been derived from the high-resolution photography. Cell widths were measured using peak detection within intensity profiles extracted along the laminar region of the cavity leading edge. Ten images were used to derive s for each combination of Re and σ photographed.

The variation of s as a function of Re , with σ as a parameter, is shown in Figure 8. As noted above, a cavity can be sustained for a lower Re with decreasing σ . The data for the two lowest σ values have an initial increase in s to a maximum at a Re of about 0.8×10^6 . With increasing Re beyond these maxima s monotonically decreases for all σ values converging to about 3.2 mm for $Re > 1.3 \times 10^6$. There is insufficient data to determine whether σ has an effect on s .

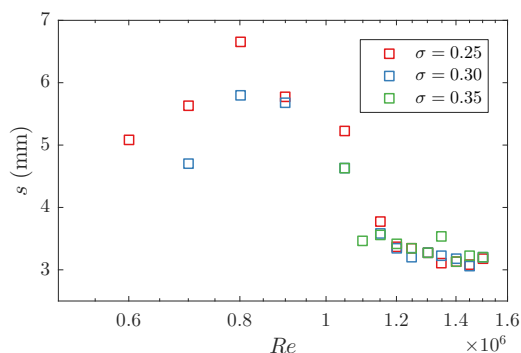
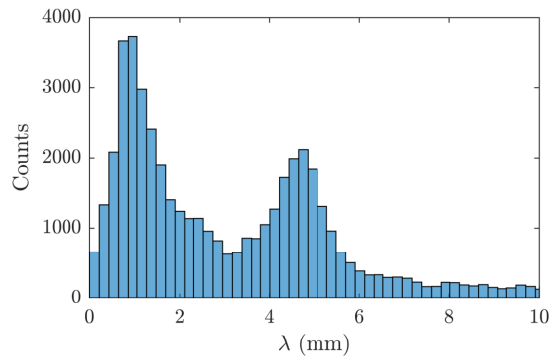


Figure 8. Average span of the cavity leading-edge cells, s , as a function of Re , with σ as a parameter denoted by symbol color.

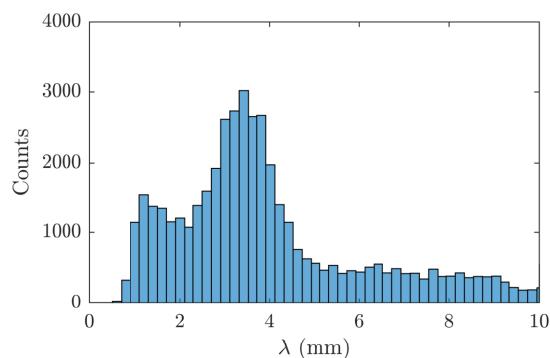
Examination of the high-speed photography shows the cells to be in a state of dynamic equilibrium undergoing constant cycles of growth and division. Wider cells preferentially grow wider with smaller neighboring cells reducing in width ultimately being washed downstream within the divot or inter-cellular secondary flow.

Autocorrelation was used to find the most probable streamwise length of periodic features, which in this case is the wavelength of the surface features. The maximum non-zero peak of the autocorrelation function was recorded for each row in each image, then compiled to form a histogram. Histograms for the two photographs shown in Figure 7 are given in Figure 9. Two peaks are evident in each case. The peak near 4 mm corresponds to the wavelength of the cavity surface waves, which may be confirmed by inspection of the photographs (Figure 7). The lower peak around 1 mm is related to the small-scale features superimposed on the large scale surface waves.

The same technique was used to measure



(a) $Re = 0.6 \times 10^6$, $\sigma = 0.25$



(b) $Re = 1.5 \times 10^6$, $\sigma = 0.25$

Figure 9. Typical histograms showing the distribution of wavelengths of cavity surface features for the two cases in Figure 7. The peaks at 4.7 mm (a) and 3.4 mm (b) correspond to the wavelengths of the shear-layer structures. The lower peaks at 0.9 mm (a) and 1.2 mm (b) are associated with the small-scale structures.

the wavelength of the surface features from the high-speed photography. As the high-speed photography is of lower spatial resolution than the still images, 3000 images were acquired for each case. The data from the high-speed and still photography show reasonable comparison (Figure 10). The wavelength of the KH waves are seen to be mild functions of both Re and σ . The wavelength of the surface waves increase with increasing σ and decreasing Re . The smaller scale features increase in wavelength with increasing Re but appear to be independent of σ .

The dynamics of the cavity surface waves were analysed using the high-speed photography. Time-series of each pixel intensity were processed

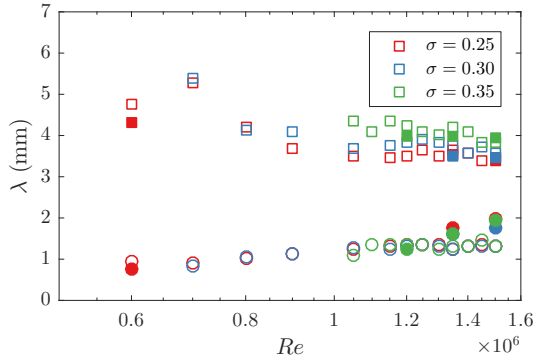


Figure 10. Wavelengths of cavity surface features as a function of Re . Different σ are denoted by colour. Solid symbols are data gathered from the high speed photography, while empty symbols are from still photography. Squares are the wavelength of the coherent structures, and circles are the small-scale features.

using a Welch periodogram with Hanning windows. Two sample spectra are shown in Figure 11. The peak frequency was extracted for each pixel position in the video, and then averaged across the continuous cavity surface.

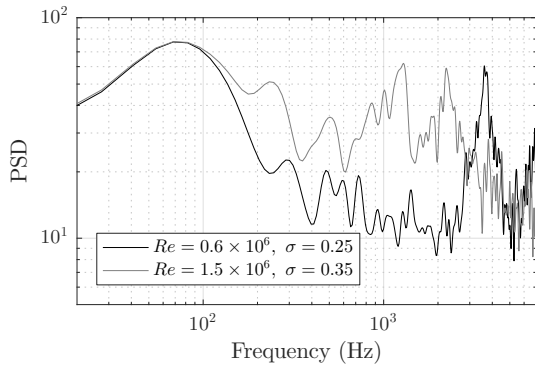


Figure 11. Typical spectra of the pixel intensity for two cases: $Re = 1.5 \times 10^6$, $\sigma = 0.25$ and $Re = 0.6 \times 10^6$, $\sigma = 0.35$.

The peak frequency for each condition was extracted and is shown in Figure 12 as a function of Re . It is unclear whether the frequency follows a linear relationship with Re , or if the surface-wave frequency follows a power law. The data shows a slight increase in frequency with decreasing σ at higher Re values.

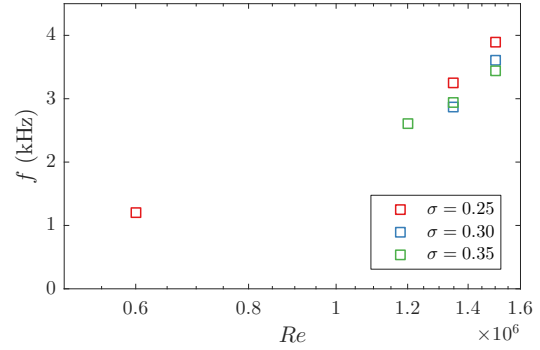


Figure 12. Cavity surface wave frequency as it varies with Re . Different σ are denoted by symbol colour.

Scaling of wake microbubble populations

The microbubble size distributions measured from the shadowgraphy for a range of Re and σ values are presented in Figures 13 and 14. The dominant bubble size was between 10 and 15 μm for all cases. Volumetric concentrations corresponding to each of these bubble number density distribution functions are given in Table 1. These data reveal that the distribution shape remains similar for all Re and σ values tested. From Figure 13 and Table 1, it can be seen that the concentration increases with Re , supporting the qualitative description of Figure 7 which were taken at a lower σ of 0.25.

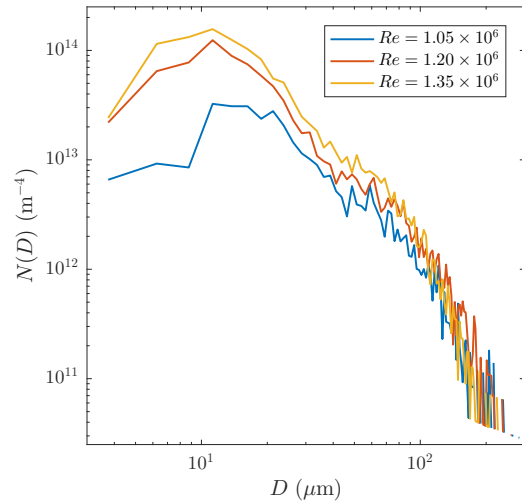


Figure 13. Bubble number density distribution function recorded for three different Re at $\sigma = 0.30$. A bin size of 2.5 μm is applied to 1000 images recorded at mid-span, 2.5 chord-lengths downstream of the hydrofoil mid-chord.

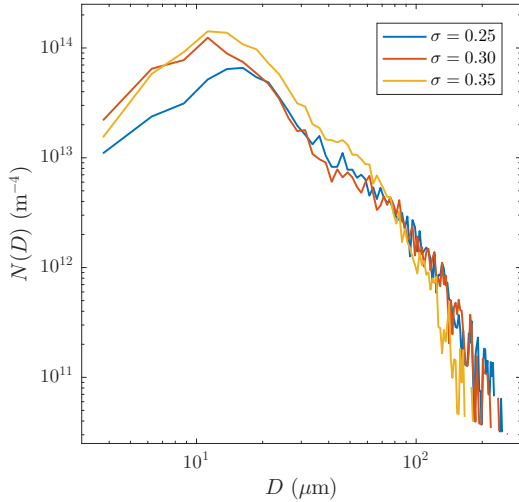


Figure 14. Bubble number density distribution function recorded for three different cavitation numbers all at $Re = 1.2 \times 10^6$. A bin size of $2.5 \mu\text{m}$ is applied to 1000 images recorded at mid-span, 2.5 chord-lengths downstream of the hydrofoil mid-chord.

Table 1. Total bubble concentrations per mm^3 for the range of bubble sizes measured. These correspond to each case displayed in Figures 13 and 14.

$Re \times 10^6$	$\sigma = 0.35$	$\sigma = 0.30$	$\sigma = 0.25$
1.05		0.84	
1.20	2.76	2.03	1.58
1.35		2.83	

The void fraction of the measured bubble populations are shown in Table 2. It should be noted that these are only representative of the range of bubble diameters measured. A true void fraction would include all the bubble sizes in the flow. There is an increase in void fraction with decreasing σ but the bubble concentration decreases indicating greater concentrations of larger bubbles. This is supported by the distribution seen in Figure 14. This trend of void fraction follows the changing scales of cavity lengths as described qualitatively above, with the breakup region lengthening as the cavitation number is decreased. The increase in void fraction can be attributed to this growth in cavity volume and the associated larger scale of the shed structures. No clear trend is apparent with Re .

Table 2. Contributed void fraction for the range of bubble sizes measured. These correspond to each case displayed in Figures 13 and 14.

$Re \times 10^6$	$\sigma = 0.35$	$\sigma = 0.30$	$\sigma = 0.25$
1.05		0.069%	
1.20	0.073%	0.107%	0.116%
1.35		0.091%	

CONCLUSIONS

The influence of Reynolds and cavitation numbers on the development of sheet cavity geometry and topography, and subsequent breakup and microbubble generation has been studied experimentally both qualitatively and quantitatively. The cavity leading edge is composed of laminar cells resulting from a complex interaction between the separating unstable boundary layer and interfacial effects. The reduction in cell size with increase in Reynolds number tends to converge for values greater than 1.3×10^6 . Waves develop in the overlying laminar boundary layer due to the Kelvin-Helmholtz instability that drive coherent breakup of the cavity trailing edge into cavitating vortical filaments. With downstream advection the filaments condense and break up into microbubbles of incondensable gas in the far wake. The scale or wavelength of the instabilities is mildly dependent on the Reynolds and cavitation numbers. The volume of shed vortices and the concentrations of the microbubbles generated increase with Reynolds number. With decreasing cavitation number the microbubble concentration decreases whereas the void fraction increases indicating a greater production of larger diameter bubbles. The dominant bubble size was found to be between 10 and 15 μm for all cases.

ACKNOWLEDGMENTS

This project was supported by the Defence Science and Technology Group (Mr. Brendon Anderson and Dr. David Clarke), the University of Tasmania, and the US Office of Naval Research (Dr. Ki-Han Kim, Program Officer) and ONR Global (Dr. Woei-Min Lin) through NICOP S&T Grant no. N62909-15-1-2019.

References

- Balachandar, S., and Eaton, J.K., "Turbulent dispersed multiphase flow," Annual Review of Fluid Mechanics, Vol. 42, 2010, pp. 111-133.
- Brandner, P.A., Lecoffre, Y., and Walker, G.J., "Development of an Australian National Facility for Cavitation Research," In Sixth International Symposium on Cavitation CAV2006, Wageningen, The Netherlands, 2006, pp. 1-9.
- Brandner, P.A., Lecoffre, Y., and Walker, G.J., "Design Considerations in the Development of a Modern Cavitation Tunnel," In 16th Australasian Fluid Mechanics Conference, 2007, pp. 630-637.
- Brandner, P.A., Walker, G.J., Niekamp, P.N., and Anderson, B., "An experimental investigation of cloud cavitation about a sphere," Journal of Fluid Mechanics, Vol. 656, 2010a, pp. 147-176.
- Brandner, P.A., Wright, G., Pearce, B., Goldsworthy, L., and Walker, G.J., "An experimental investigation of microbubble generation in a confined turbulent jet," In 17th Australasian Fluid Mechanics Conference, 2010b.
- Castro, A.M., Li, J., Hyman, M., and Carrica, P.M., "Turbulent and cavity free surface bubble entrainment with application to ship hydrodynamics," In 30th Symposium on Naval Hydrodynamics, Hobart, Australia, 2014.
- de Graaf, K.L., Zarruk, G.A., Brandner, P.A., and Pearce, B.W., "Microbubble Content in the Wake of a Cavitating Hydrofoil," In 19th Australasian Fluid Mechanics Conference, 2014, pp. 1-4.
- Deane, G.B., and Stokes, M.D., "Scale dependence of bubble creation mechanisms in breaking waves," Nature, vol. 418, 2002, pp. 839-844.
- Doolan, C., Brandner, P.A., Butler, D., Pearce, B., Moreau, D., and Brooks, L., "Hydroacoustic characterisation of the AMC Cavitation Tunnel," In Acoustics 2013 - Science, Technology and Amenity, Victoria Harbour, Australia, 2013.
- Fox, R.O., "Large-eddy-simulation tools for multiphase flows," Annual Review of Fluid Mechanics, Vol. 44, 2012, pp. 47-76.
- Ganesh, H., Mäkiharju, S.A., and Ceccio, S.L., "Partial cavity shedding due to the propagation of shock waves in bubbly flows," In 30th Symposium on Naval Hydrodynamics, Hobart, Australia, 2014.
- Gnanaskandan, A. and Mahesh, K., "Large eddy simulation of sheet to cloud cavitation," In 30th Symposium on Naval Hydrodynamics, Hobart, Australia, 2014.
- Gnanaskandan, A. and Mahesh, K., "A numerical method to simulate turbulent cavitating flows," International Journal of Multiphase Flow, Vol. 70, 2015, pp. 22-34.
- Huang, B., Ducoin, A., and Young, Y.L., "Physical and numerical investigation of cavitating flows around a pitching hydrofoil," Physics of Fluids, Vol. 25, No. 10, 2013, 102109.
- Ji, B., Luo, X., Wu, Y., Peng, X., and Duan, Y., "Numerical analysis of unsteady cavitating turbulent flow and shedding horse-shoe vortex structure around a twisted hydrofoil," International Journal of Multiphase Flow, Vol. 51, 2013, pp. 33-43.
- Ji, B., Peng, X.X., Long, X.P., Luo, X.W., and Wu, Y.L., "Numerical evaluation of cavitation shedding structure around 3D Hydrofoil: Comparison of PANS, LES and RANS results with experiments," In Journal of Physics: Conference Series, Vol. 656, conference 1, 2015, 012127.
- Karn, A., Ellis, C., Hong, J., and Arndt, R.E.A., "Investigations into the turbulent bubbly wake of a ventilated hydrofoil: Moving toward improved turbine aeration techniques," Experimental Thermal and Fluid Science, Vol. 64, 2015, pp. 186-195.
- Kim, D., Mani, A., and Moin, P., "Investigation of bubble formation by breaking waves in turbulent two-phase Couette flows," In 30th Symposium on Naval Hydrodynamics, Hobart, Australia, 2014.
- Kjeldsen, M., Arndt, R.E.A., and Effertz, M., "Spectral characteristics of sheet/cloud cavitation," Journal of Fluids Engineering, Vol. 122, No. 3, 2000, pp. 481-487.
- Liao, Y., and Lucas, D., "A literature review of theoretical models for drop and bubble breakup in tur-

bulent dispersions,” Chemical Engineering Science, Vol. 64, No. 15, 2009, pp. 3389-3406.

Liao, Y., and Lucas, D., “A literature review on mechanisms and models for coalescence processes of fluid particles,” Chemical Engineering Science, Vol. 65, No. 10, 2010, pp. 2851-2864.

Maeda, M., Yamaguchi, H., and Kato, H., “Laser holography measurement of bubble population in cavitation cloud on a foil section,” In First ASME-JSME Fluids Engineering Conference, Portland, OR, 1991, pp. 23-27.

Qin, Q., Song, C.C.S., and Arndt, R.E.A., “A numerical study of the unsteady turbulent wake behind a cavitating hydrofoil,” In Fifth International Symposium on Cavitation (Cav2003) Osaka, Japan, 2003a.

Qin, Q., Song, C.C.S., and Arndt, R.E.A., “Incondensable gas effect on turbulent wake behind a cavitating hydrofoil,” In Fifth International Symposium on Cavitation (Cav2003) Osaka, Japan, 2003b.

Smith, R.W., and Peterson, R.S., “Dynamic and diffusive growth of microbubbles near a two-dimensional hydrofoil,” IEEE Journal of Oceanic Engineering, Vol. 9, No. 2, 1984, pp. 93-97.

Song, C. and He, J. “Numerical simulation of cavitating flows by single-phase flow approach” 3rd Int. Symp. on Cavitation Grenoble, France 1998.

Song, C. and Qin, Q. “Numerical simulation of unsteady cavitating flows” Proc. Fourth Int. Symp. Cavitation, Pasadena, California, 2001.

Tassin Leger, A., Bernal, L.P., and Ceccio, S.L., “Examination of the flow near the leading edge of attached cavitation: Part 2. Incipient breakdown of two-dimensional and axisymmetric cavities,” Journal of Fluid Mechanics, Vol. 376, 1998, pp. 91-113.

Washuta, N., Masnadi, N., and Duncan, J., “The turbulent boundary layer on a horizontally moving partially submerged, surface-piercing vertical wall,” In 30th Symposium on Naval Hydrodynamics, Hobart, Australia, 2014.

Yu, P.-W., and Ceccio, S.L., “Diffusion induced bubble populations downstream of a partial cavity,” Journal of Fluids Engineering, Vol. 119, No. 4, 1997, pp. 782-787.

1 Discussion

Simo A. Mkiharju
Flow, Offshore and Waves Laboratory (FLOW lab)
University of California, Berkeley

The authors are to be congratulated for impressive work, and for a paper that was a pleasure to read.

1. The reader would be curious to know if the authors have had a chance to also study how sensitive the bubble number density distribution (discussed in connection to figures 13 and 14) is to the spanwise location. Looking at figure 2 and some of the frames in figure 5, there seems to be some variation and it would be interesting to know if the number density is uniformly decreasing, or does the mean bubble size also vary depending on the spanwise location?
2. While the remaining incondensable gas bubbles in the wake have more complex origins than canonical bubble breakup in shear, are the trends observed in the bubble sizes for various Re relatable to something similar to the Hinze scaling?

2 Authors' Reply

We thank the Reviewer for their comments.

Question 1 There is some variation in the spanwise bubble density however not near our measurement locations for this foil. Our research in this area has been iterative. An earlier publication by de Graaf, et al. (2014) examined the span-wise microbubble concentration for a single tunnel operating condition, contained within this study. They found that the total number plateaued across a region near the center span. This region was roughly between 40-65% of the total length (span) of the foil. There is however an increase in the dominant bubble size towards the root and tip. As the same foil is being used we may be confident the distribution and concentration does not alter greatly near the centre-span of the foil and consequently the region surrounding our shad-

owgraphy measurements (see figure 2). At present we are interested in how the upstream cavitation topology affects the downstream populations and so we benefit from the consistency of this central region. However, outside the present investigation a more detailed picture of this variation would be of interest and we look to examine this in the future.

Question 2 The variation of bubble sizes appears to vary similar to that for bubble breakup in turbulence where the Hinze scale defines sizes for which surface tension overcomes inertia. However in this case the evolution of the ultimate bubble size in the wake from its original formation is more complicated in that it involves the breakup of the cavity trailing edge followed by mass transfer, by condensation and potentially gaseous diffusion. As we have shown the turbulence scales involved at cavity breakup vary with the Reynolds number such that the balance of surface tension and inertial forces is affected. However no features can be discerned from the spectra that would suggest any particular feature is changing with the Reynolds number other than the overall changes discussed. We nevertheless thank the discussor for this interesting question.

3 Discussion

Roger E. A. Arndt
St. Anthony Falls Laboratory
University of Minnesota

The authors are to be complemented for their excellent paper on sheet/cloud cavitation. One of the significant features of the paper is the careful documentation of the bubbly wake. For example, Figures 6 and 7 illustrate the significant effect of Reynolds number on wake structure over a relatively narrow range of 0.6×10^6 to 1.5×10^6 at $\sigma = 0.25$. A question remains on any influence of dissolved gas. Kjeldsen, et al. (2000) showed the wake structure was significantly modified by dissolved gas coming out of solution to form gas bubbles that were slow to dissolve, unlike vapor bubbles that readily condensed as assumed in the numerical models developed at our laboratory by Song and He. This led to an improved numerical model by taking this into account (Qin et al 2003a, 2003b). However gas content was not varied in these early experiments. With the new tunnel gas content and nuclei content can be varied independently. This may provide an interesting extension of the current research.

Generally speaking there is little documentation in the literature of the effects of gas content on sheet/cloud cavitation. Our research indicated that differences in gas content were found to significantly alter the lift spectrum of a cavitating foil. For a certain range of $\sigma/2\alpha$ near 4, the dominant oscillation frequency appears to double when the gas content is reduced by a half. The effect of gas content is illustrated in the accompanying figure that contains the outtake of high speed video. This difference can be used to explain some of the discrepancies observed between tunnels. The new tunnel provides a significant opportunity to study this effect.

4 Authors' Reply

We thank the Reviewer for these detailed comments. The effects of dissolved gas and nuclei content is indeed of considerable interest. The results presented here are the precursor for further investi-

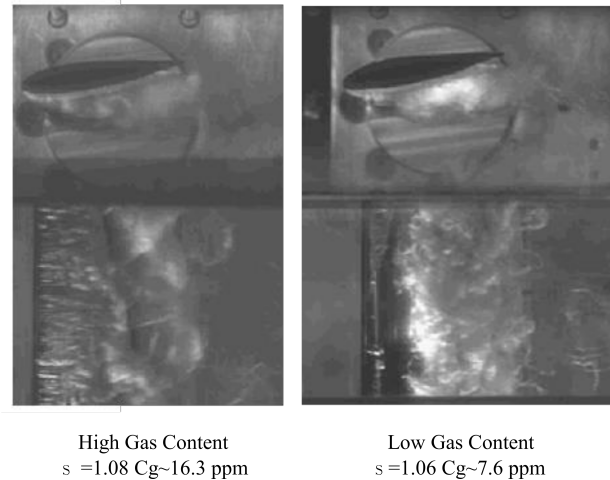


Figure 15. Effect of gas content on cavitation, (provided by Discusser).

gation in this area. As noted there is some literature in this area, but experimental results in particular are not widely reported and prove to be challenging to obtain (Kjeldsen, et al. (2000); Song and He (1998); Song and Qin (2001); Qin, et al. (2003a,b)). Controlling both these quantities independently in experiments will provide a wealth of information and with this baseline complete we look forward to extending this research in the future.